Catalysis Letters
https://doi.org/10.1007/s10562-020-03472-w

# Fe Doped MIL-101/Graphene Nanohybrid for Photocatalytic Oxidation of Alcohols Under Visible-Light Irradiation

**Mingming Wang**[1] · **Yali Ma**[1] · **Bolin Lv**[1] · **Fenglin Hua**[1] · **Shuangyan Meng**[1] · **Xuedi Lei**[1] · **Qingtao Wang**[1] · **Bitao Su**[1] · **Ziqiang Lei**[1] · **Zhiwang Yang**[1]

Received: 24 September 2020 / Accepted: 16 November 2020

## Abstract

A novel photoactive porous material of GR/FeMIL-101 based on FeMIL-101 metal organic frameworks (MOFs) was successfully synthesized via a simple hydrothermal method. The structural and photoelectric properties of the GR/FeMIL-101 was analyzed by XRD, SEM, TEM, TGA, XPS, UV–vis DRS, FT-IR, PL and EIS methods. The photocatalytic performance for the selective oxidation of benzyl alcohol with GR/FeMIL-101 as catalysts was evaluated under visible light irradiation. The results showed that the GR/FeMIL-101 nanohybrid had better photocatalytic performance than both of FeMIL-101 and the pristine MIL-101. It was further found that the incorporation of Fe and MIL-101 caused valence fluctuations of $Fe^{3+}/Fe^{2+}$ which improved the absorption of visible-light and increased the separation efficiency of photogenerated charges. In addition, the combination of FeMIL-101 and GR could further promote the transfer rate of the photoelectrons. The mechanism of the reaction revealed that $\cdot O_2^-$ was the dominating active specie in this reaction through active species trapping experiments.

### Graphic Abstract

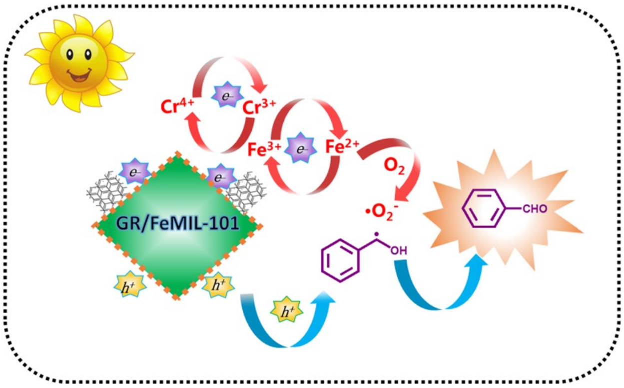

**Scheme** proposed photocatalytic mechanism of GR/FeMIL-101(Cr) under visible irradiation

Fe doped MIL-101/GR nanohybrid was successfully synthesized as an efficient photocatalyst for selective oxidation of alcohols under visible-light and shown a best conversion of 50%. Analyses revealed that Fe was successfully doped into the MIL-101, valence fluctuation of Fe2+/Fe3+ not only improved the visible-light absorption but also increased the separation rate of photoexcited carriers. Graphene further improved the transportation rate of electron (e-). Subsequently, the possible photocatalytic mechanism for the selective oxidation of alcohols was proposed. It was proved that superoxide radicals (·O2-) was the main active species when the reaction was performed under Oxygen atmosphere.

**Keywords** GR/FeMIL-101 · Photocatalytic · Benzyl alcohol · Oxidation · Visible light · Mofs

---

✉ Zhiwang Yang
yangzw@nwnu.edu.cn

Extended author information available on the last page of the article

## 1 Introduction

Nowadays, with the development and progress of human society, the problems of energy shortage and environmental pollution have become two major challenges for people. Rich and clean solar energy has been attracted the attentions of many researchers [1–3]. The heterogeneous photocatalysis can effectively utilize solar energy to solve these two major problems. Therefore, it offers many possibilities for the development of semiconductor photocatalytic technology. It's worth noting that the nanomaterials based on metal organic frameworks (MOFs) have a great potential for visible light photocatalytic reactions [4–6]. For instance, Wang et al. reported an aromatic heterocycle-grafted photocatalytic material of $NH_2$-MIL-125(Ti) for selectively oxidizes alcohol under visible light. The results indicated that the aromatic heterocycle-grafted MOFs exhibited a significant activity for oxidation of alcohols under visible light [7].

As we know, MOFs are porous coordination materials formed by transition-metal ions or metal clusters with organic linkers [8–10]. In recent years, because of the excellent structural characteristics such as large specific surface area, large active center, porosity and flexible structure tunability, MOFs have been widely used in gas storage and separation [11], drug carriers [12], sewage treatment [13], photocatalytic conversion of organic compounds [14, 15] electrocatalysis [16] and fluorescence sensing [17]. Moreover, MIL-101 is one of the promising metal organic framework materials with a regular octahedral structure and a larger specific surface area (2191 $m^2g^{-1}$) as well as a high stability in air or strong acid solutions. It has been applied to gas separation [18], degradation of dye pollutants [19], photocatalytic hydrogen generation [20]. As a photocatalytic material, MIL-101 can absorb visible-light due to its narrow band gap (2.06 eV) [21]. However, the material with narrow $E_g$ is not absolutely good for the separation of electrons and holes. Therefore, it is significant to explore how to improve the photocatalysis of MIL-101. We found that the partial suitable metal ions, as an electron mediator in the nodes, can greatly improve the photocatalytic performance via decreasing the recombination rate of charge efficiently by valence fluctuation. Yamashita et al. reported that the Ce ions were successfully doped in the nodes of MIL-101 and promoted $H_2$ production under visible light irradiation [22]. According to the above researches, it can be seen that doping redoxactive (multi) metallic nodes such as Fe, Mn, Ni, Co, Cu and Ce is an effective method to improve the photocatalytic performance of MOFs [23]. In the previous works of our group, a series of Fe ions doped UiO-66 nanoparticles were successfully synthesized to enhance photocatalytic activity under visible-light for selectively aerobic oxidation of aromatic alcohols [24] and the degradation performance [25]. However, it is also important to study the effect of Fe on the photocatalytic properties of other MOFs materials.

In this work, the Fe-doped MIL-101 catalyst was successfully synthesized by a simple hydrothermal method and the photocatalytic performance was improved after the doping of Fe species. Then, the GR/FeMIL-101 nanohybrid was obtained by the combination of the prepared FeMIL-101 and graphene (GR) to further improve the photocatalytic activity of selective oxidation of benzyl alcohol under visible light. The possible mechanism of GR/FeMIL-101 photocatalytic process was also explored by trapping experiments and Mott-Schottky plots measurements.

## 2 Experimental

### 2.1 Materials

All the chemical reagents used in this research were analytically pure purchased from the commercial companies, and directly employed without further purification.

### 2.2 Preparation of Photocatalysts

Graphene oxide (GO) nanostructure was obtained according to the literature [26]. 0.5 g graphite was firstly dispersed in 12 mL $H_2SO_4$ (95%) solution and was being stirred at − 5 °C, then 1.5 g $KMnO_4$ was added into the solution, the mixture was ultrasonically treated for 12 h at room temperature. The resulted suspension was quickly transferred to 15% $H_2O_2$ aqueous solution and continuously stirred for 2 h. After the reaction, the solid was collected by centrifugation and washed several times with $H_2O$ until pH 7, and then it was freeze-dried for further using.

MIL-101 was synthesized through a simple hydrothermal method according to the literature [27]. Briefly, 0.48 g $Cr(NO_3)_3{\cdot}9H_2O$, 0.2 g 1,4-terephthalic acid and 22 μL hydrofluoric acid (40%) were added to 6 mL $H_2O$ and stirred for 30 min at room temperature, then the solution was transferred to a Teflon-lined stainless steel autoclave and maintained at 220 °C for 8 h. After being cooled to room temperature, the obtained mixture was centrifuged at 8000 r/min and washed several times with DMF and anhydrous ethanol. Then, in order to activate MIL-101, the as-prepared sample was dispersed in 50 mL ethanol and transferred to 65 mL autoclave which was then being kept at 90 °C for 20 h. Finally, after naturally cool down, the obtained MIL-101 was washed by ethanol several times and dried at 160 °C for 8 h to remove the surplus DMF. FeMIL-101 was synthesized and activated by the same way just as the synthesis of

MIL-101 but adding 0.2 mmol $FeCl_3·6H2O$ to the aqueous solution.

GR/FeMIL-101 nanohybrid was obtained by thermal treating as the follow process. 3.0 mg GO was ultrasonically dispersed in 2 mL $H_2O$ and added to 6 mL aqueous solution including 0.48 g $Cr(NO_3)_3·9H_2O$, 0.2 g 1,4-benzene dicarboxylic acid, 22 μL hydrofluoric acid (40%) and 0.2 mmol $FeCl_3·6H2O$. After being stirred for 30 min, the mixture solution was transferred to a Teflon-lined stainless steel autoclave and heated at 220 °C for 8 h. At last, after being purified and activated, GR/FeMIL-101 nanohybrid was obtained.

## 2.3 Catalyst Characterization

X-ray powder diffraction (XRD) patterns of the samples were recorded on a Rigaku D/Max-2400 with Cu Kα radiation. Fourier transform infrared (FT-IR) spectroscopy was carried on a Nicolet NEXUS 670 with the scanning range from 400 to 4000 $cm^{-1}$. The photoluminescence (PL) spectra of the samples were conducted with the excitation wavelength of 450 nm on a PELS-55 luminescence/fluorescence spectrophotometer. UV–vis diffuse reflectance spectra (UV–vis DRS) of the samples were characterized by a Cary 500 UV–vis NIR spectrophotometer. X-ray photoelectron spectroscopy (XPS) method was used to analyze the elements of the catalysts by a Thermo VG Scientific Sigma Probe instrument with an Al Kα radiation. $N_2$ adsorption desorption isotherms of the samples were carried on an Autosorb-iQ2-MP instrument. The thermogravimetric analysis (TGA) was conducted on a TA Instruments Discovery Thermo gravimetric Analyzer from 25 to 800 °C at the rate of 10 °C $min^{-1}$ in $N_2$ atmosphere. SEM images were observed through a Carl Zeiss Ultra Plus scanning electron microscope. TEM images were measured by a $TECNAIG^2$ transmission electron microscope. Electrochemical impedance spectroscopy (EIS) was performed on PGSTAT302N workstation to observe chemical properties of the samples.

## 2.4 Evaluations of Photocatalytic Activity

A 500 W xenon lamp with a 400 nm cut off filter was used to get the wave length (λ) greater than 400 nm visible light to test the photocatalytic oxidation activity of catalysts at room temperature. Firstly, 10 mg catalyst and 0.1 mmol alcohols were added into a quartz vial. Then the reactor was treated under ultrasound for 1 min and shaken to make sure that the catalyst was evenly dispersed in the solvent. Afterwards, the reacted solution was kept under dark for 2 h in order to insure that the construction of the alcohols' adsorption and desorption equilibriums on the catalyst surface. In the end, the samples were irradiated under visible light for 8 h. After the photocatalytic reaction, the conversion and the selectivity of the alcohols were obtained by the follow formulas:

$$\text{Conversion of the alcohol (\%)} = \left[\left(C_0 - C_n\right)/C_0\right] \times 100$$

$$\text{Selectivity of the aldehyde/ketone (\%)} = \left[C_a/\left(C_0 - C_n\right)\right] \times 100$$

where $C_0$ is the concentration of alcohol before irradiation, $C_n$ and $C_a$ is the concentration of alcohol and aldehyde/ketone after irradiation via gas chromatograph (Shimadzu GC-2010) analysis.

# 3 Results and Discussions

## 3.1 Characterization

The X-ray powder diffraction (XRD) was used to characterize the crystal and phase structure of the samples. The XRD patterns of MIL-101, FeMIL-101, GO and GR/FeMIL-101 were shown in Fig. 1. The spectrum of pristine MIL-101 can be great fitted with the simulated MIL-101, indicating the successful synthesis of MIL-101 [29]. FeMIL-101 maintained the similar characteristic peaks as the pure MIL-101, and no additional reflection of Fe presented, indicating the doping Fe into MIL-101 did not change the framework structure and no new phase of Fe compounds formed [22, 29]. It was worthy to pay attention that the XRD peaks of GR/FeMIL-101 were similar to that of MIL-101 and FeMIL-101, but the peaks intensity slightly decreased. It was ascribe to the successful combining of GR and FeMIL-101.

The FT-IR spectra of MIL-101, FeMIL-101 and GR/FeMIL-101 nanocomposites were showed in Fig. 2. For MIL-101, the peaks at the range of 2825–3687 $cm^{-1}$ were attributed to the crystalline water and the OH groups in the ligand of $H_2BDC$. The peaks at 1405–1610 $cm^{-1}$ were ascribed to the stretching vibrations of C=C bonds. The

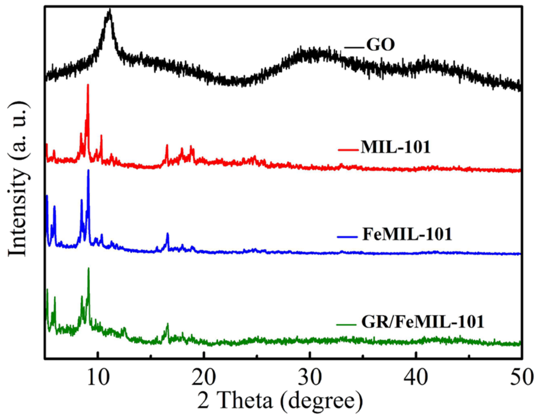

**Fig. 1** XRD patterns of the samples

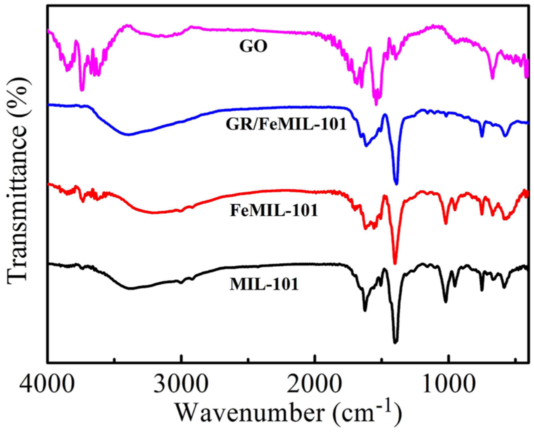

**Fig. 2** FT-IR spectra of the samples

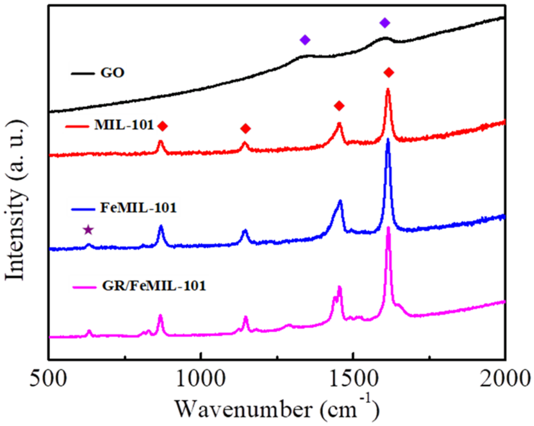

**Fig. 3** Raman spectra of the samples

peak at 1400 cm$^{-1}$ was linked to the symmetric stretching of O=C=O groups in the carboxylate group of the BDC ligand. The peak with medium strength at 580 cm$^{-1}$ was due to the vibrations of Cr–O bonds, which proved that MIL-101 had been formed. For GO, the peak at 1720 cm$^{-1}$ was assigned to the C=O stretching vibration, and the peak at 692 cm$^{-1}$ was ascribed to the absorption signals of epoxide group [26]. The FT-IR spectra of FeMIL-101 and GR/FeMIL-101 were in common with that of the pure MIL-101, which indicated that the framework of FeMIL-101 and GR/FeMIL-101 were not affected by the doping of Fe and combination of GR [29–32].

Figure 3 showed the Raman spectra of the obtained samples. The GO sample exhibited two characteristic bands at 1337 cm$^{-1}$ and 1587 cm$^{-1}$ while MIL-101 had four characteristic bands at 1611, 1453, 1142, and 866 cm$^{-1}$. As for the spectrum of FeMIL-101, besides the main bands of MIL-101, the band at 629 cm$^{-1}$ could be assigned to the oxidation state of Fe [31]. The successful incorporation of Fe into the MIL structure without preventing MIL crystal formation was proved. In the case of GR/FeMIL-101, besides the main bands of FeMIL-101, the band at 1336 cm$^{-1}$ was ascribed to the GO which indicated FeMIL-101 was coated by the GR layers.

Figure 4a showed the UV–vis DRS absorption properties of the samples. The absorption edge around 300 nm was ascribed to the π-π* electronic jumping of the aromatic ring and the absorption in the visible region was ascribed to the *d-d* spined transition of $Cr^{3+}$ in MIL-101 [22]. Compared with the pure MIL-101, there was a great red shift of FeMIL-101 caused by the doping of Fe into the crystal structure of MIL-101. Moreover, GR/FeMIL-101 had obvious enhanced absorption due to the good pristine visible light absorption of carbon materials [10, 26, 28, 34].

The photoluminescence (PL) spectra can give the separation efficiency of the charges in the photocatalysts [10, 26, 28]. As shown in Fig. 4b, we could find that the PL emission intensity of GR/FeMIL-101 was far lower than those of MIL-101 and FeMIL-101, which clearly indicated that the doping of Fe into MIL-101 could efficiently promote the separation of photo-generated carriers. And the excellent charges separation efficiency was somewhat due to not only the own photoelectronic performance but also the excellent conductivity of GR [28, 33].

XPS data of GR/FeMIL-101 were shown in Fig. 5. The XPS survey scanning indicated the atom content of the O,

**Fig. 4** UV–vis DRS (**a**) and PL spectra of the samples (**b**)

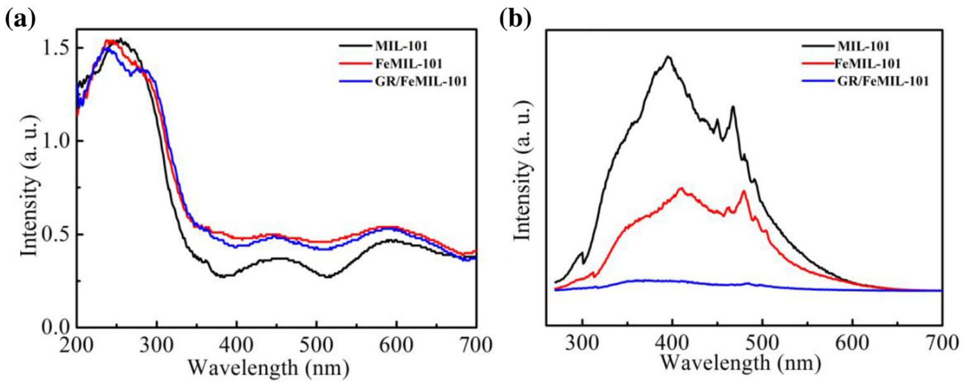

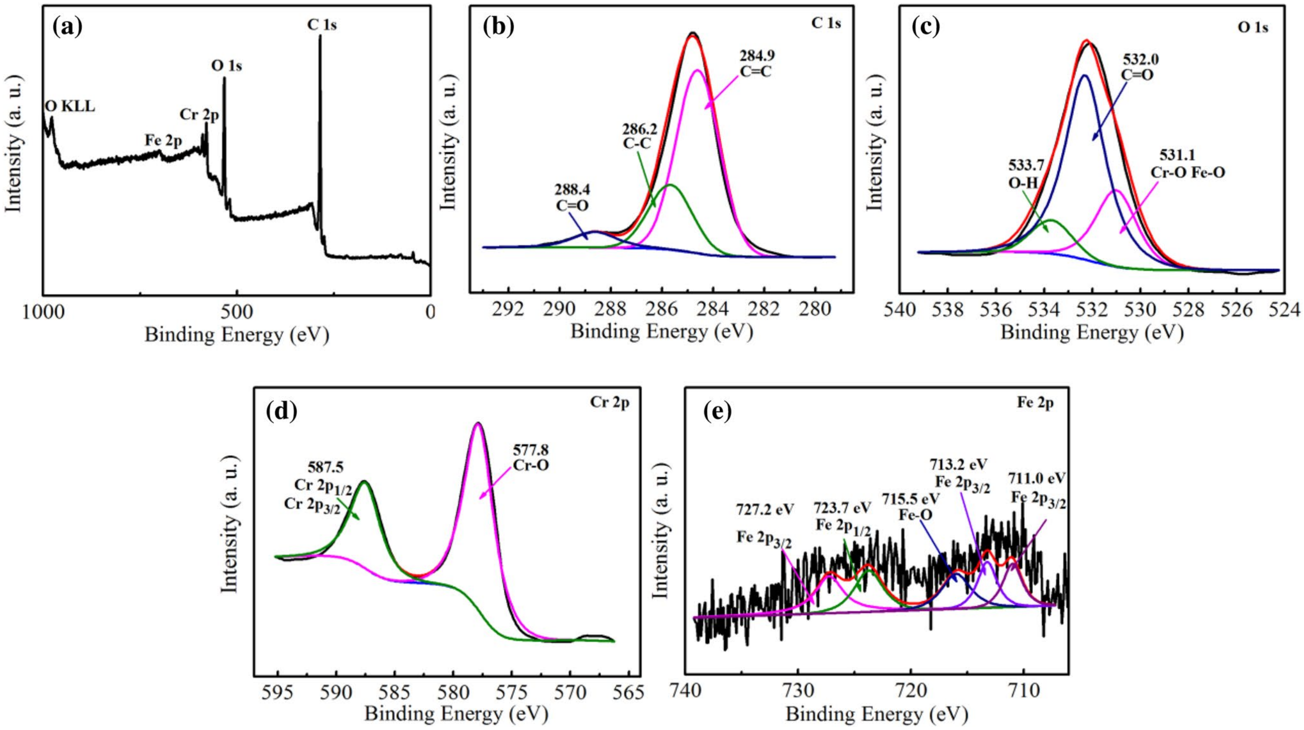

**Fig. 5** XPS spectra of GR/MIL-101: survey (**a**); C1s (**b**); O1s (**c**); Cr2p (**d**) and Fe2p (**e**)

C, Cr and Fe on the surface of GR/FeMIL-101 were 73.98%, 21.35%, 4.48% and 0.19%, respectively (Fig. 5a). Inductively couple plasma (ICP) was also carried out to study the content of Fe element. The result calculated was 0.21% which was close to the result of XPS. In the XPS spectrum of C1s, the fitted peaks at 284.9 eV, 288.4 eV and 286.2 eV can be attributed to the C=C, C=O and C–C bond from $H_2BDC$ in the framework of FeMIL-101, respectively (Fig. 5b). For the spectrum of O1s, the peaks at 532.0 eV and 533.7 eV was related to the signals of C=O and O–H groups, respectively. And the peak at 533.1 eV represented the Cr–O and Fe–O species (Fig. 5c). Figure 5d presented the XPS spectra of Cr2p. It was found that the spectra of Cr2p showed two peaks at 577.8 eV and 587.5 eV, which were corresponding to the $Cr2p_{1/2}$ and $Cr2p_{3/2}$ signals, respectively. The Fe2p core level spectrum consists of $Fe2p_{3/2}$ and $Fe2p_{1/2}$ excitations. The XPS signals of GR/FeMIL-101 revealed the existence of the $Fe^{2+}$. The peak at 711.0 eV was for $Fe2p_{3/2}$, and the peak at 723.7 eV was for $Fe2p_{1/2,}$ respectively. The peak at 715.5 eV also proved the existence of Fe–O species in GR/FeMIL-101 nanocomposites (Fig. 5e). These data were well in agreement with the reported results [24, 35].

$N_2$ adsorption–desorption isotherms of the samples were shown in Fig. 6. The $N_2$ adsorption–desorption curves of the samples were shown in Fig. 6a and the average pore diameters of the samples were shown in Fig. 6b. The specific surface area of the pure MIL-101 was 4397 $m^2g^{-1}$, and the average pore diameter was 2.23 nm. The specific surface

**Fig. 6** Nitrogen adsorption–desorption isotherms (**a**) and pore size distribution curves (**b**) of the samples

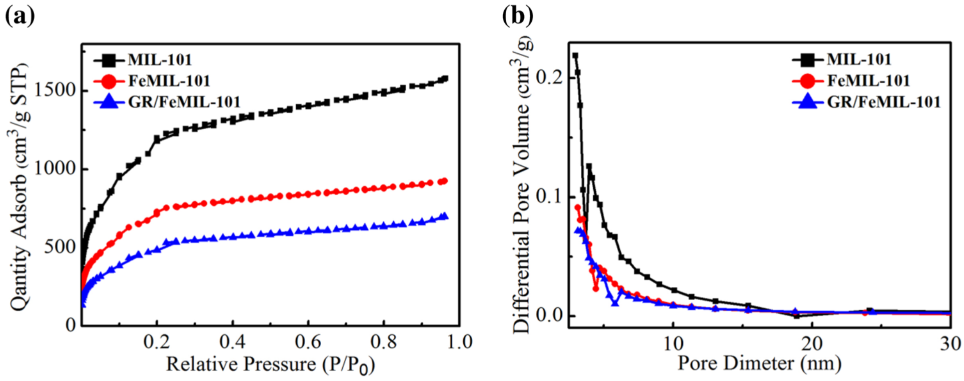

area of FeMIL-101 was found to be 2554 $m^2g^{-1}$, and the average pore diameter was 2.24 nm. It showed an obvious change of the surface area of FeMIL-101 after the doping of Fe into MIL-101, indicating that the introducing of Fe would change the framework but a lot of micropores were still existed in FeMIL-101. The specific surface area decreased again when GR was combined with FeMIL-101. It showed that the specific surface area of GR/FeMIL-101 decreased to 1851 $m^2g^{-1}$ due to a small number of GR entered into the aperture of FeMIL-101. However, the average pore diameter maintained during the combination. The average pore diameter of FeMIL-101 was 2.35 nm.

Thermogravimetric analyses (TGA) of MIL-101, FeMIL-101, GR/FeMIL-101 and GO were shown in Fig. 7. For all catalysts, during the initial stage of heating up to the temperature of 100 °C, a rapid weight loss occurred due to the removal of water from the larger cage of MOFs and GO. For MIL-101, FeMIL-101 and GR/FeMIL-101, the second stage which was observed in the temperature range of 100–300 °C was related to the removal of DMF solvent from the crystal structure of MIL-101. As for pure MIL-101, during the temperature range of 300–480 °C, the observed weight loss was corresponded to the collapse of crystal structure [36]. When Fe was doped into MIL-101, the stability of FeMIL-101 was significantly increased, and the collapse occurred at the temperature range of 400–520 °C. The stability of GR/FeMIL-101 was further improved when FeMIL-101 was combined with GR due to the good compatibility as well as the strong molecular interaction between FeMIL-101 and GR.

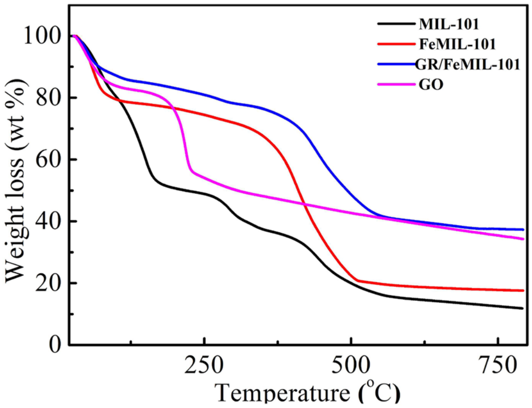

**Fig. 7** TGA profiles of the samples

The SEM images of the samples at different magnification times were shown in Fig. 8. Most of the samples were basically octahedral pyramid shaped. It was noted that FeMIL-101 presented a rough surface obviously compared with pure MIL-101 after the doping of Fe into MIL-101. For GR/FeMIL-101, it maintained the adhesive morphology due to GR attaching on the surface of FeMIL-101.

The morphology of MIL-101 and GR/FeMIL-101 were also observed by TEM as shown in Fig. 9. MIL-101 showed regular octahedral morphology with a smooth surface. However, the images of GR/FeMIL-101 sample were very different from the images of MIL-101. From the images of GR/FeMIL-101 sample, after the doping Fe, a rough surface could be seen, and it was clear that a number of GR were well dispersed on the surface of FeMIL-101. These results

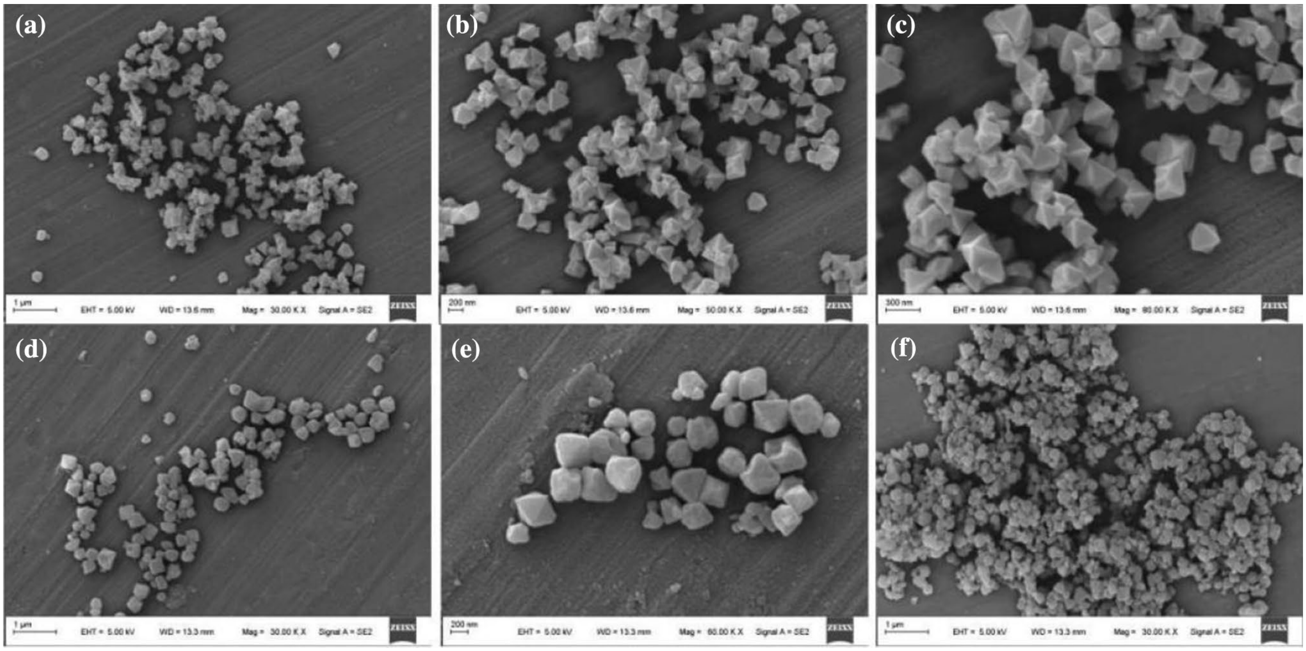

**Fig. 8** SEM images for MIL-101 (**a**, **b**, **c**), FeMIL-101 (**d**, **e**) and GR/FeMIL-101 (**f**)

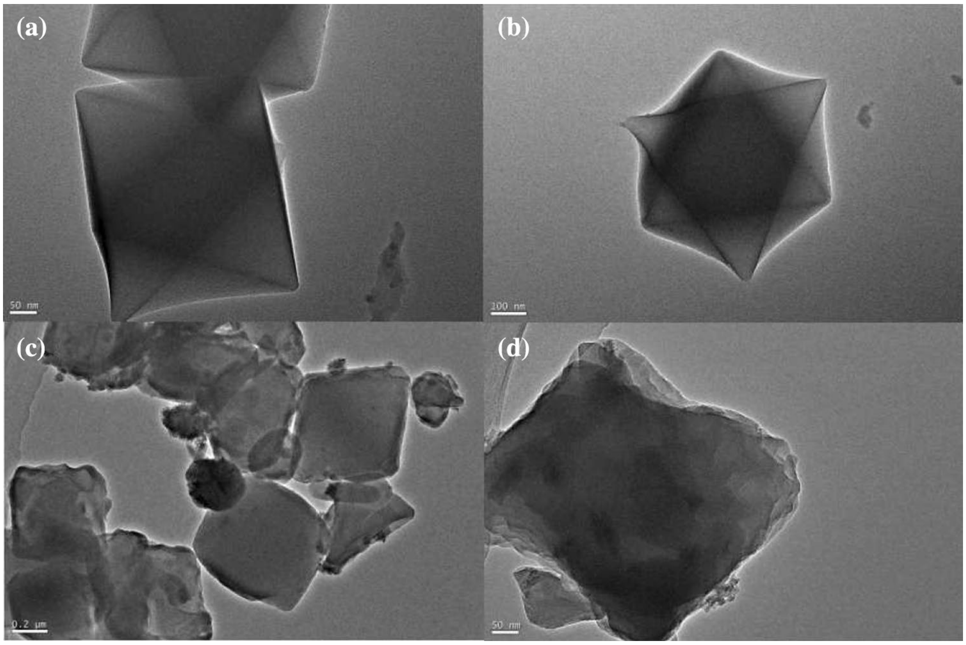

**Fig. 9** TEM images of MIL-101 (**a**, **b**) and GR/FeMIL-101 (**c**, **d**)

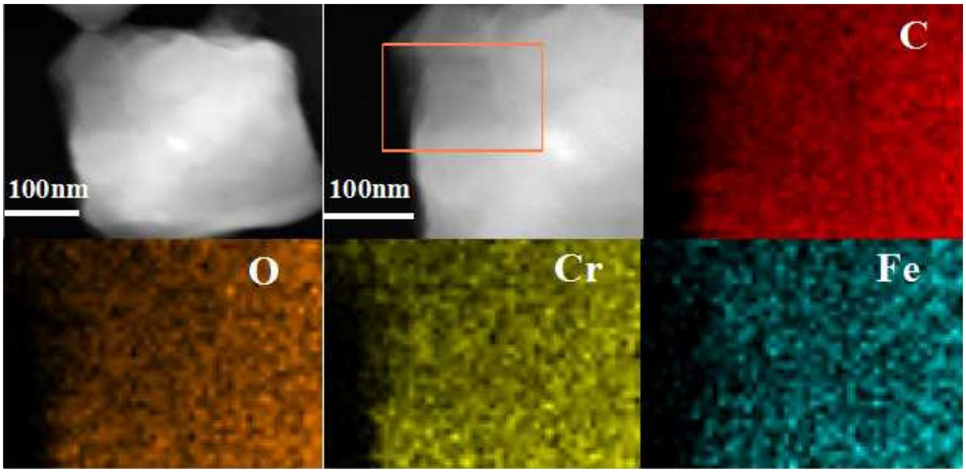

**Fig. 10** The EDS pictures of GR/FeMIL-101

suggested that the heterojunctions between GR and FeMIL-101 were formed, which would improve the charge separation and transfer efficiency of the photoinduced carriers.

The component of GR/FeMIL-101 nanocomposite was further investigated by the TEM EDS characterization shown in Fig. 10. It found that the materials were composed of C, O, Cr, and Fe elements which were evenly distributed over the surface of GR/FeMIL-101.

EIS Nyquist plots of MIL-101, FeMIL-101 and GR/FeMIL-101 were shown in Fig. 11. The arcs reflected the charge-transfer resistance at the surface of the electrode. The smaller arc radius indicated that a faster interfacial charge transfer and an effective separation of the photo-generated electron–hole pairs occurring in a photocatalyst [37, 38]. From the Fig. 11 we could find that FeMIL-101 had a much smaller arc radius than the pure MIL-101, while GR/

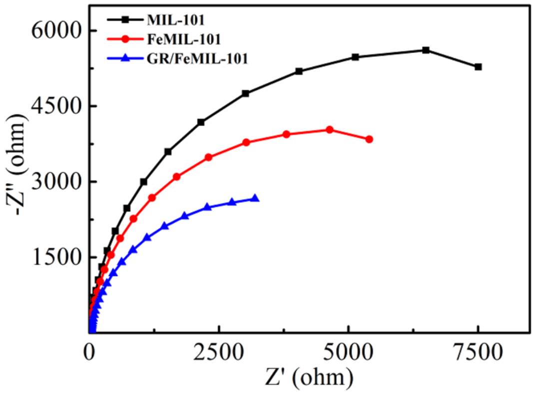

**Fig. 11** EIS Nyquist plots of samples

**Table 1** Photocatalytic oxidation of benzyl alcohol with different catalysts

| Entry[a] | Catalyst | Con. (%)[b] | Sel. (%)[c] |
|---|---|---|---|
| 1 | none | 0 | / |
| 2 | MIL-101 | 4 | 99 |
| 3 | FeMIL-101 | 25 | 99 |
| 4 | GR/FeMIL-101 | 50 | 99 |
| 5[d] | GR/FeMIL-101 | 3 | 99 |

[a] Conditions: 10 mg catalyst, 0.1 mmol benzyl alcohol, ethyl acetate 10 mL, light $\lambda > 400$ nm, reaction time 8 h

[b,c] The conversion (Con. %) and the selectivity (Sel. %) were calculated by GC analysis (similarly hereinafter)

[d] Without visible light irradiation

**Table 2** Photooxidation of benzyl alcohol in different solvents

| Entry | Solvent | Con. (%) | Sel. (%) |
|---|---|---|---|
| 1 | Carbon tetrachloride | 5 | 98 |
| 2 | Ethyl acetate | 50 | 99 |
| 3 | 1, 2-Dichloroethane | 25 | 98 |
| 4 | Acetone | 34 | 98 |
| 5 | Ethanol | 5 | 99 |
| 6 | Acetonitrile | 15 | 99 |
| 7 | Isopropanol | 8 | 99 |
| 8 | $H_2O$ | 14 | 99 |

Conditions: catalyst 10 mg, benzyl alcohol 0.1 mmol, light $\lambda > 400$ nm, solvent 10 mL, reaction time 8 h

FeMIL-101 had a smallest arc radius among all the samples, suggesting the most excellent charge transferred efficiency over the surface of GR/FeMIL-101.

## 3.2 Photocatalytic Performance

The photocatalytic activity of the prepared catalysts was tested by the photocatalytic oxidation of benzyl alcohol with visible light irradiation. The controlling experiment was also carried out under the identical conditions. The results were summarized in Table 1.

The results in Table 1 showed that poor catalytic activity with the only 4% conversion of benzyl alcohol could be observed for MIL-101. The weak catalytic activity of single MIL-101 could be due to the low charge separation efficiency. However, doping Fe into MIL-101 greatly improved the conversion of benzyl alcohol (Table 1, entry 3). Obviously, the conversion for the catalysis of GR/FeMIL-101 reached 50% under the same conditions, proving that the combination of GR could effectively improve the photocatalytic activity of the catalyst.

The photooxidation of benzyl alcohol was carried out in different solvent under identical reaction conditions, and the corresponding results were listed in Table 2. It was obvious that ethyl acetate was an ideal solvent in this photocatalytic system, and the highest conversion of 50% could be reached in the photooxidation.

The polarity of the solution was an important factor in the catalytic reaction. As the polarity of the solution increased, the conversion rate of benzyl alcohol decreased (Table 2, entry 2, 4, 5, 7). The polarity of acetonitrile is greater than that of ethanol but the conversion of benzyl alcohol in acetonitrile was higher than in ethanol (Table 2, entry 5, 6). This phenomenon was due to the nitrile group of acetonitrile accelerating the oxidation of alcohol. Carbon tetrachloride, as the electron capture agent, will trap electrons and block the production of the superoxide radical ($\cdot O_2^-$), so that the conversion of benzyl alcohol was just 5% (Table 2, entry 1). Meanwhile, the weaker trapping electron of 1, 2-dichloroethane caused the conversion of benzyl alcohol in 1, 2-dichloroethane was lower than that in ethyl acetate but higher than that in carbon tetrachloride (Table 2, entry 1, 2, 3).

The substrate expansion results with the catalysis of GR/FeMIL-101 were summarized in Table 3. It showed that all the photooxidations afforded high aldehyde selectivity more than 98%, however, moderate conversions not high than 60% were provided for all the reactions. The substituents on the aromatic rings and the molecular structure had complex effect on all the photooxidations. Both the electron-donating group and the electron-withdrawing group have effects on the conversion of benzyl alcohol. According to the mechanism, the free radical is the key species in the oxidation. And only a single electron exists in the p orbit of the center carbon in the free radical. When the benzene ring is attached to an electron-donating group, the single electron in the p orbital of the center carbon in the benzyl group will be partially paired with the electron from the electron-donating group, and which would make it more stable. On the other hand, as for the benzene ring with the electron-withdrawing group, the single electron in the p orbit will be transferred to the electron-withdrawing group and the electron density of the p orbit will be somewhat empty, so that the p orbit was also relatively stable. The scopes for the application of GR/FeMIL-101 were worthy to further investigations.

The stability of GR/FeMIL-101 in the photooxidation of benzyl alcohol was investigated and shown in Fig. 12. It showed after three times of parallel experiments, the catalyst still maintained good catalytic activity for the oxidation. This meant that GR/FeMIL-101 had good stability in this photocatalytic system.

In order to further confirm the stability of GR/FeMIL-101 structure, XRD and FT-IR of GR/FeMIL-101 before and after the photocatalytic reaction were investigated and shown in Fig. 13. The XRD patterns (Fig. 13a) and FT-IR spectra (Fig. 13b) of GR/FeMIL-101 sample had quite little changes

**Table 3** Photooxidation of various substituted benzyl alcohols over GR/FeMIL-101 under visible light irradiation

| Entry | Substrate | Product | Con. (%) | Sel. (%) |
|---|---|---|---|---|
| 1 | 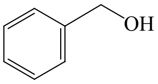 | 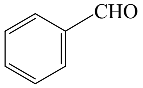 | 50 | 98 |
| 2 | 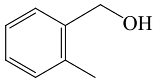 | 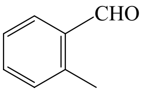 | 10 | 99 |
| 3 | 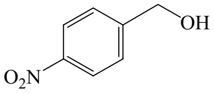 | 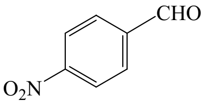 | 11 | 98 |
| 4 | 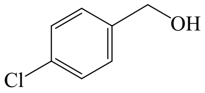 | 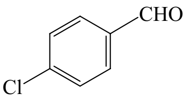 | 46 | 98 |
| 5 | 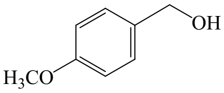 | 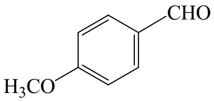 | 38 | 98 |
| 6 | 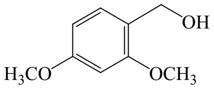 | 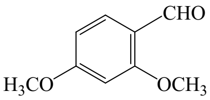 | 21 | 99 |
| 7 | 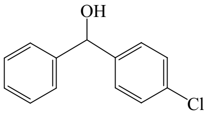 | 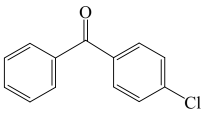 | 30 | >99 |
| 8 | 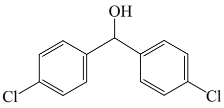 | 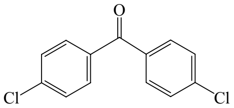 | 57 | >99 |
| 9 | 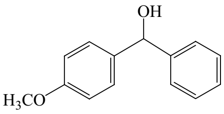 | 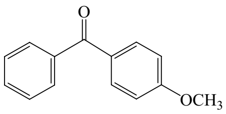 | 37 | >99 |
| 10 | 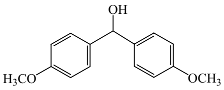 | 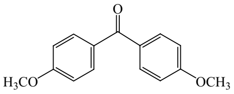 | 42 | >99 |

Conditions: GR/FeMIL-101 10 mg, substrate 0.1 mmol, ethyl acetate 10 mL, light λ > 400 nm, reaction time 8 h

after catalytic reaction. This implied that the structure of GR/FeMIL-101 remained intact after at least three times of parallel experiments and the stability of the composite was further proved.

### 3.3 Reaction Mechanisms

In order to explain the possible photocatalytic mechanism of the photocatalytic oxidation of alcohol with the catalysis of GR/FeMIL-101, some controlled experiments were operated with different radical scavengers. To measure the effect of ·OH radicals, isopropyl alcohol (IPA) was for removing ·OH. Ethylenediamine tetraacetic acid disodium (EDTA-2Na), $AgNO_3$ and 1, 4-benzoquinone (BQ) were also used as the scavengers for the capturing of $h^+$, $e^-$, and superoxide radical ($\cdot O_2^-$), respectively [26, 39, 40], the results were shown in Fig. 14a. When BQ, $AgNO_3$ and $N_2$ were added, the conversion of benzyl alcohol was sharply decreased.

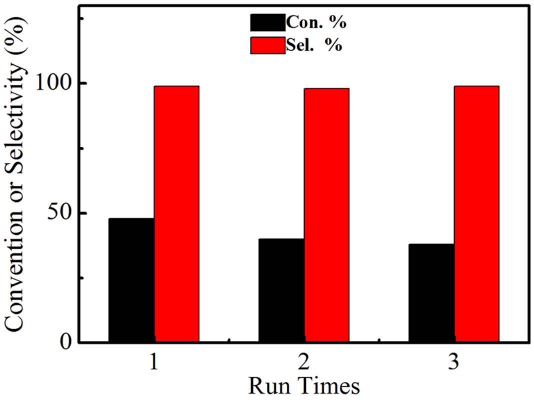

Fig. 12 The recycling property of GR/FeMIL-101 for the photooxidation of benzyl alcohol

When EDTA-2Na and IPA were added into the reaction, the conversion decreased slightly. It suggested that ·OH and $h^+$ was not vital in the reaction. As a result, it was obvious that $\cdot O_2^-$ was the main activity species in this photocatalytic process.

Mott-Schottky plots were measured and shown in Fig. 14b. It was clear that the flat band position of FeMIL-101 is − 0.56 V *vs* Ag/AgCl (− 0.30 V *vs* NHE). According to UV–vis DRS characterization, the absorptions wavelength edge of FeMIL-101 was 600 nm, and the corresponding calculated $E_g$ of FeMIL-101 was 2.07 eV. Hereby, the estimated potential positions of CB and VB of FeMIL-101 were − 0.46 V and 1.58 V *vs* NHE, respectively [41, 42].

According to the previous researches, the oxidation potential of $O_2/O_2^-$ was − 0.33 V *vs* NHE, therefor, the CB potential (− 0.46 V) of FeMIL-101 was capable to reduce $O_2$ to oxygen radicals ($\cdot O_2^-$). The VB of FeMIL-101 was 1.58 V, which was not enough to oxidize benzyl alcohol completely, but to form active intermediate. Moreover, the catalyst was not enough to generate ·OH radicals (2.4 V *vs*. NHE, pH 7) under visible light [43, 44]. So we could find that the concentration of ·OH did not show significant impact on the photooxidation. Based on these findings, a possible mechanism was proposed and illustrated in Scheme 1.

When GR/FeMIL-101 was exposed to a visible light irradiation condition, $e^-$ and $h^+$ generated in the catalyst. With the reduction of $Cr^{4+}$ and $Fe^{3+}$ ions by the photoinduced $e^-$, $\cdot O_2^-$ was produced subsequently. Simultaneously, benzyl alcohol was oxidized by the photoinduced $h^+$ to produce new benzyl radicals. The newly produced benzyl radicals were then immediately oxidized by the $\cdot O_2^-$, and benzaldehyde formed successfully. It showed that $\cdot O_2^-$ was very important for this photocatalytic process.

Fig. 13 XRD patterns (**a**) and FT-IR spectra (**b**) of GR/FeMIL-101 before and after the catalytic reactions

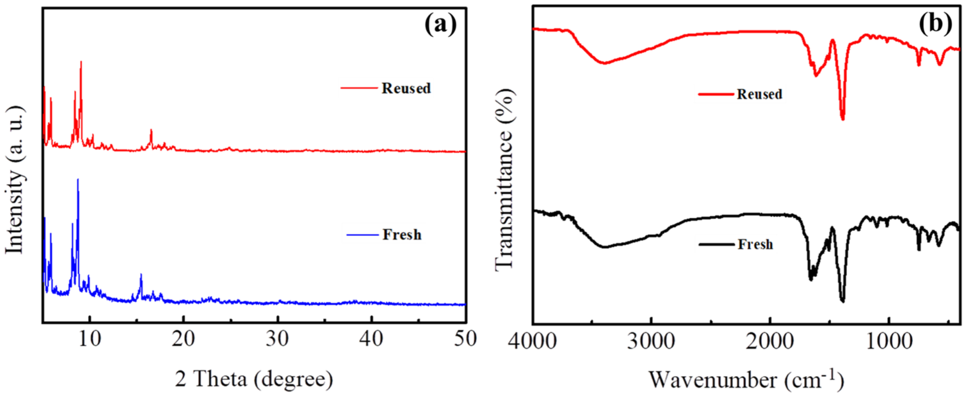

Fig. 14 The species capturing results (**a**) and the Mott-Schottky plot (**b**) for the photooxidation of benzyl alcohol with the catalysis of GR/FeMIL-101

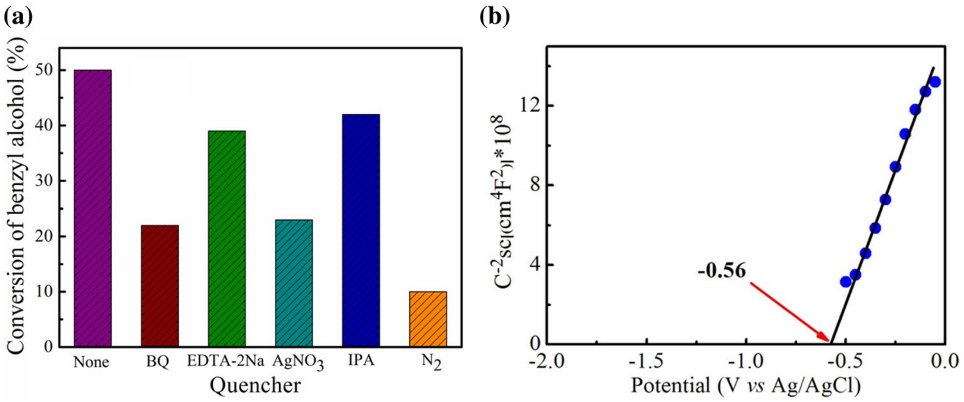

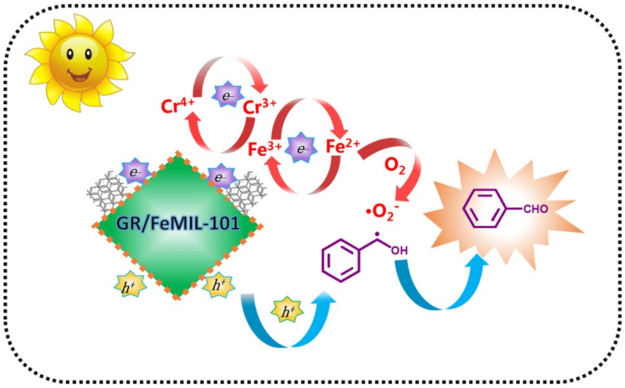

**Scheme 1** Possible mechanism for the photocatalytic oxidation of alcohols over GR/FeMIL-101

## 4 Conclusions

In summary, the nanohybridized GR/FeMIL-101 was successfully prepared by a simple hydrothermal method, which showed the moderate catalytic activity for the phooxidation of benzyl alcohol under visible light irradiation. It certified that the doping of Fe to MIL-101 and the combination of GR with FeMIL-101 really could improve the charge separation efficiency of the catalyst. The mechanism revealed that $\cdot O_2^-$ was the dominating active species for the photooxidation of benzyl alcohol. This photocatalytic system was worthy of further investigations to apply the prepared photocatalyst to other photocatalytic reactions.

**Acknowledgements** The research was financially supported by NSFC (52063026, 21563026), the Program for Changjiang Scholars and Innovative Research Team in University (IRT15R56), the Innovation Team Basic Scientific Research Project of Gansu Province (1606RJIA324), and the Science and Technology Program of Gansu Province (19JR2RA020). We also thank the Key Laboratory of Eco-functional Polymer Materials (Northwest Normal University), Ministry of Education, and the Gansu International Scientific and Technological Cooperation Base of Water-Retention Chemical Functional Materials, for financial support.

## References

1. Zhao Y, Ding C, Zhu J, Qin W, Tao X, Fan F, Li R, Li C (2020) Angew Chem Int Ed 59:9653–9658
2. Rahman MZ, Kibria MG, Mullins CB (2020) Chem Soc Rev 49:1887–1931
3. Jiao X, Zheng K, Hu Z, Sun Y, Xie Y (2020) ACS Cent Sci 6:653–660
4. Diercks CS, Liu Y, Cordova KE, Yaghi OM (2018) Nat Mater 943:301–307
5. Zhu Y, Yin J, Hamad EA, Liu X, Chen W, Yao T, Mohammed OF, Alshareef HN (2020) Adv Mater 32:1906368
6. Liu R, Meng S, Ma Y, Niu L, He S, Xu X, Su B, Lu D, Yang Z, Lei Z (2019) Catal Commun 124:108–112
7. Wu Z, Huang X, Zheng H, Wang P, Hai G, Dong W, Wang G (2018) Appl Catal B 224:479–487
8. Meng S, Zeng W, Wang M, Niu L, Hu S, Su B, Yang Y, Yang Z, Xue Q (2020) New J Chem 44:2102–2110
9. Hanikel N, Prévot MS, Yaghi OM (2020) Nat Nanotechnol 15:348–355
10. Yang Z, Xu X, Liang X, Lei C, Wei Y, He P, Lv B, Ma H, Lei Z (2016) Appl Catal B 198:112–123
11. Adil K, Belmabkhout Y, Pillai RS, Cadiau A, Bhatt PM, Assen AH, Maurin G, Eddaoudi M (2017) Chem Soc Rev 46:3402–3430
12. Doonan C, Riccò R, Liang K, Bradshaw D, Falcaro P (2017) Acc Chem Res 50:1423–1432
13. Soltani R, Marjani A, Shirazian S (2020) Dalton Trans 49:5323–5335
14. Liu H, Xu C, Li D, Jiang H (2018) Angew Chem Int Ed 57:5379–5383
15. Meng S, Wang M, Lu B, Xue Q, Yang Z (2019) Acta Chim Sin 77:1184–1193
16. Pan Y, Sun K, Liu S, Cao X, Wu K, Cheong W, Chen Z, Wang Y, Li Y, Liu Y, Wang D, Peng Q, Chen C, Li Y (2018) J Am Chem Soc 140:2610–2618
17. Qu F, Sun C, Lv X, You J (2018) Microchim Acta 185:4597–4602
18. Rajati H, Navarchian AH, Tangestaninejad S (2018) Chem Eng Sci 185:92–104
19. Jiang Z, Feng L, Zhu J, Li X, Chen Y, Khan S (2020) Ceram Int 46:19084–19091
20. Wang Y, Zhang Y, Jiang Z, Jiang G, Zhao Z, Wu Q, Liu Y, Xu Q, Duan A, Xu C (2016) Appl Catal B 185:307–314
21. He J, Yan Z, Wang J, Xie J, Jiang L, Shi Y, Yuan F, Yu F, Sun Y (2013) Catal Commun 49:6761–6763
22. Wen M, Kuwahara Y, Mori K, Zhang D, Li H, Yamashita H (2015) J Mater Chem 3:14134–14141
23. Fu Y, Sun L, Yang H, Xu L, Zhang F, Zhu W (2016) Appl Catal B 187:212–217
24. Xu X, Liu R, Cui Y, Liang X, Lei C, Meng S, Ma Y, Lei Z, Yang Z (2016) Appl Catal B 187:484–494
25. Ma Y, Liu R, Meng S, Niu L, Yang Z, Lei Z (2019) Acta Chim Sin 77:153–159
26. Sun L, Du T, Hu C, Chen J, Lu J, Lu Z, Han H (2017) ACS Sustain Chem Eng 5:8693–8701
27. Hong D, Hwang YK, Serre C, Férey G, Chang J (2009) Adv Funct Mater 19:1537–1552
28. Yang Z, Xu X, Liang X, Lei C, Gao L, Hao R, Lu D, Lei Z (2017) Appl Surf Sci 420:276–285
29. Zheng Y, Chu F, Zhang B, Yan J, Chen Y (2018) Microporous Mesoporous Mater 263:71–76
30. Hupp JT, Poeppelmeier KR (2005) Science 309:2008–2009
31. Nirumand L, Farhadi S, Zabardasti A, Khataee A (2018) Ultrason Sonochem 42:647–658
32. Guo H, Su S, Liu Y, Ren X, Guo W (2020) Environ Sci Pollut Res 27:17194–17204
33. Liu J, Xu H, Xu Y, Song Y, Lian J, Zhao Y, Wang L, Huang L, Ji H, Li H (2017) Appl Catal B 207:429–437
34. Han X, He X, Sun L, Han X, Zhan W, Xu J, Wang X, Chen J (2018) ACS Catal 8:3348–3356
35. Vu TA, Le GH, Dao CD, Dang LQ, Nguyen KT, Dang PT, Tran HTK, Duong QT, Nguyen TV, Lee GD (2014) RSC Adv 4:41185–41194
36. Kayal S, Chakraborty A (2018) Chem Eng J 334:780–788
37. Hou Y, Zuo F, Dagg AP, Liu J, Feng P (2014) Adv Mater 26:5043–5049
38. Liu R, He X, Niu L, Lv B, Yu F, Zhang Z, Yang Z (2019) Acta Chim Sin 77:653–660
39. Ding J, Xu W, Wan H, Yuan D, Chen C, Wang L, Guan G, Dai WL (2018) Appl Catal B 221:626–634

40. Bi J, Zhou Z, Chen M, Liang S, He Y, Zhang Z, Wu L (2015) Appl Surf Sci 349:292–298
41. Yuan Y, Yin L, Cao S, Xu G, Li C, Xue C (2015) Appl Catal B 168:572–576
42. Huang T, Hua Y, Yao J, Luo Y, Liu X (2018) Mater Chem Phys 212:506–512
43. Ye X, Chen Y, Ling C, Zhang J, Meng S, Fu X, Wang X, Chen S (2018) Chem Eng J 348:966–977
44. Bibi R, Shen Q, Wei L, Hao D, Li N, Zhou J (2018) RSC Adv 8:2048–2058

## Affiliations

**Mingming Wang[1] · Yali Ma[1] · Bolin Lv[1] · Fenglin Hua[1] · Shuangyan Meng[1] · Xuedi Lei[1] · Qingtao Wang[1] · Bitao Su[1] · Ziqiang Lei[1] · Zhiwang Yang[1]**

[1] Key Laboratory of Polymer Materials of Gansu Province, Key Laboratory of Eco-Functional Polymer Materials, Ministry of Education, College of Chemistry and Chemical Engineering, Northwest Normal University, Lanzhou 730070, China